Article:

Ye, J. orcid.org/0000-0002-6857-7450, Liu, Y., Yang, Y. et al. (3 more authors) (2023) Testing, analysis and design of wire and arc additively manufactured steel bolted connections. Engineering Structures, 296. 116939. ISSN 0141-0296

https://doi.org/10.1016/j.engstruct.2023.116939

Testing, analysis and design of wire and arc additively manufactured steel bolted connections

Jun Ye[5], Yunyi Liu[1], Yuanzhang Yang[1], Zhen Wang[3], Ou Zhao[4], Yang Zhao[1]

1. College of Civil Engineering and Architecture, Zhejiang University, Hangzhou, 310058, China
2. Center for Balance Architecture, Zhejiang University, Hang Zhou, 310014, China
3. Department of Civil Engineering, Zhejiang University City College, Hangzhou, 310015, China
4. School of Civil and Environmental Engineering, Nanyang Technological University, Singapore
5 School of Civil Engineering, University of Leeds, Leeds, LS2 9JT, UK S

Abstract

Capitalizing on Wire and Arc Additive Manufacturing (WAAM), 3D printed steel has shown significant potential in manufacturing large-scale steel structural elements in the construction industry. Due to the intrinsic difference in material properties, the mechanical performance of WAAM steel connections requires further investigation. In this paper, a total number of 24 WAAM steel coupon specimens with three different print layer orientations and 36 WAAM single-shear bolted connection specimens with one bolt of different design configurations were fabricated, dimensionally measured with 3D scanning technique, and tested under monotonic tension. The failure modes and ultimate capacities of the bolted connections were analysed, focusing on the print layer orientations of the WAAM steel plates. The current codified design provisions and design approaches proposed in the literature for steel structures were further evaluated by comparing the failure modes and ultimate capacities of the bolted connection specimens. This research shows that specimens with different print layer orientations present anisotropy phenomena in the coupon tests and bolted connection tests with differences of up to 10% and 20%, respectively. The relatively accurate predictions of the ultimate capacity of the

WAAM steel bolted connection specimens following the current steel design standards are significantly compromised by predicting the incorrect failure modes, which could be attributed to the influence of anisotropic material properties of the WAAM steel plates and the failure modes of tilt-bearing and the end-splitting not being considered in current design provisions. This research conducted systematic experimental investigations focusing on the material properties of WAAM steel and the structural behaviours of WAAM single-shear bolted connections, which could potentially promote the application of WAAM technology in construction industry.

Keywords: 3D printing; Wire arc additive manufacturing; Single-shear bolted connections; Failure modes; Design approaches

1. Introduction

Additive manufacturing (AM), also known as 3D printing, has attracted attention from the construction industry because of its advantages in structural efficiency, geometric freedom, customization, and reduced material waste, along with high integration with digital structure designs [1]. Metal AM techniques can be classified into three major categories: Powder Bed Fusion (PBF), Directed Energy Deposition (DED), and Sheet Lamination [2]. Wire and arc additive manufacturing (WAAM), belonging to one of the DED techniques, uses traditional welding tools to form structural members with deposited welding materials [1, 3]. Compared to traditional subtractive manufacturing methods and other AM techniques, WAAM shows significant potential in the construction industry for its fast production speed, low equipment cost, high material utilization, and high sustainability [4].

The WAAM technology has been successfully used for the construction of the 3D printed footbridge [5, 6], as shown in Figure 1. The successful implementation of the 3D printed bridge demonstrated the significant potential of metal 3D technology as an alternative construction method in the building of infrastructures with complex shapes. Structurally efficient WAAM components with elegant appeal and complex shapes can be generated using topology and layout optimization [7, 8]. This also emphasizes the importance of investigations on the fundamental behaviour of 3D printed materials and components for further application in the construction industry. Several research works have been conducted to investigate the WAAM steel material properties [9-16]. For the component level, the cross-sectional behaviours of WAAM components were investigated, including Buchanan et al. [17] and Laghi et al. [18] on circular hollow section stub columns, Kyvelou et al. [19] on square hollow section stub columns, Huang et al. [20, 21] on columns with different hollow sections, and Guo et al. [22] on T-stub connections. However, the research on WAAM steel for bolted connections is still limited.

(a) (b)

Figure. 1. 3D printed bridges: (a) a MX3D metal 3D printed footbridge [5], and (b) a small 3D printed footbridge in shell form [6].

Bolted connections have already been widely used in steel construction and are the potential option to assemble large scale metal 3D printed structures. The structural behaviours of bolted connections are affected by various factors, including the contact interaction between the bolts and their surrounding holes, the elastic-plastic relationships of materials, and the effect of large deformations in the connected plates [15, 23-25]. The potential failure modes for a single-shear single-bolt connection mainly include shear-out, bearing, and net section failure (except for bolt shear) [26]. The design ultimate capacity of a bolted connection corresponding to those failure modes has been specified in the different standards of cold-formed steel design codes and guidelines, including AS/NZS 4600 [27], AS 4100 [28], AISI S100 [29], AISC 360 [30], EN 1993-1-1 [31], EN 1993-1-3 [32], and EN 1993-1-8 [33].

Design approaches for the shear connections were also proposed by researchers around the globe to achieve more efficient designs. Based on the existing standards, Teh et al. [34-38]

defined a shear lag coefficient and an active shear plane to predict the ultimate capacities of net section and shear-out failure modes, respectively, which had already been referenced by AISI S100 [29] and AS/NZS 4600 [27]. Salih et al. [39, 40] established finite element models for stainless steel bolted connections and proposed the design equations of the ultimate capacities of stainless steel bolted connections for thin steel plates. Kim et al. [41-43] found that bolt connections with thin plates under single shear were prone to out-of-plane deformations, and revised the design equations considering the curling effect. Two failure modes not mentioned in the standards, end-splitting and tilt-bearing, were observed in the experiments. Lyu et al. [44, 45] considered the end-splitting failure as the transitional failure mode between shear-out and net section failure and proposed a new equation to predict the ultimate capacities considering end-splitting failure. Distinguished from curl-bearing and localised tearing failure, a new formula was proposed by Teh and Uz [46] for the tilt-bearing failure of the bolted connections with thinner plates.

However, most of the current research works focusing on bolted connections are based on steel manufactured by conventional methods. Ding et al. [47] highlighted the uniqueness of cold-formed steel design in which local sheet bending can influence connection strength, as opposed to hot-rolled steel for which such effects are safely ignored. This means that bolted connections fabricated with different materials could show different failure modes and ultimate load-carrying capacities. Guo et al. [48] tested the ultimate load-carrying capacities and failure modes of WAAM steel single-shear bolted connections in two different nominal thicknesses, two different print layer orientations, and varying dimensions. They preliminarily analysed the mechanical characteristics of WAAM steel single-shear bolted connections and the prediction accuracy of different standards. However, more comprehensive analyses are required to be conducted based on further research and experimental data.

This paper presents an experimental programme regarding the mechanical properties and structural behaviours of WAAM steel single-shear bolted connections subjected to monotonic tension. A 3D laser scanner and a Matlab program are used to obtain the geometric properties of WAAM steel specimens with undulating surfaces as the basis for discussion of WAAM steel material properties. Twenty-four coupon specimens with three different print layer orientations are tested under tension. A total number of 36 single-shear connection specimens with one bolt with various plate dimensions, hole sizes, and hole positions were designed, fabricated from WAAM plates, and tested with DIC measuring the displacement. The failure modes and ultimate capacities of the bolted connections were analysed. The validity of the available codified design provisions and design equations proposed in the current literature for conventional thin-walled steel bolted connections were evaluated for the 3D printed steel plate connections. This research conducted systematic experimental investigations focusing on the WAAM steel specimens, which could potentially promote the application of WAAM technology in construction industry.

2. Experimental programme

2.1 Materials and specimens

WAAM steel plates of 3 mm nominal thickness were extracted from the oval tubes with flat sides manufactured using the WAAM process for the fabrication of the material and bolt connection specimens, as shown in Figure 2. The chemical compositions, mechanical properties, and printing parameters of ER50-6 low-carbon steel feedstock are listed in Table 1, Table 2, and Table 3, respectively. Although the manufacturing parameters, such as the heat input and the cooling rates, were not provided by the material supplier, the influence of the manufacturing parameters on the microstructure and material properties of the WAAM specimens could refer to the work of other researchers [10, 49].

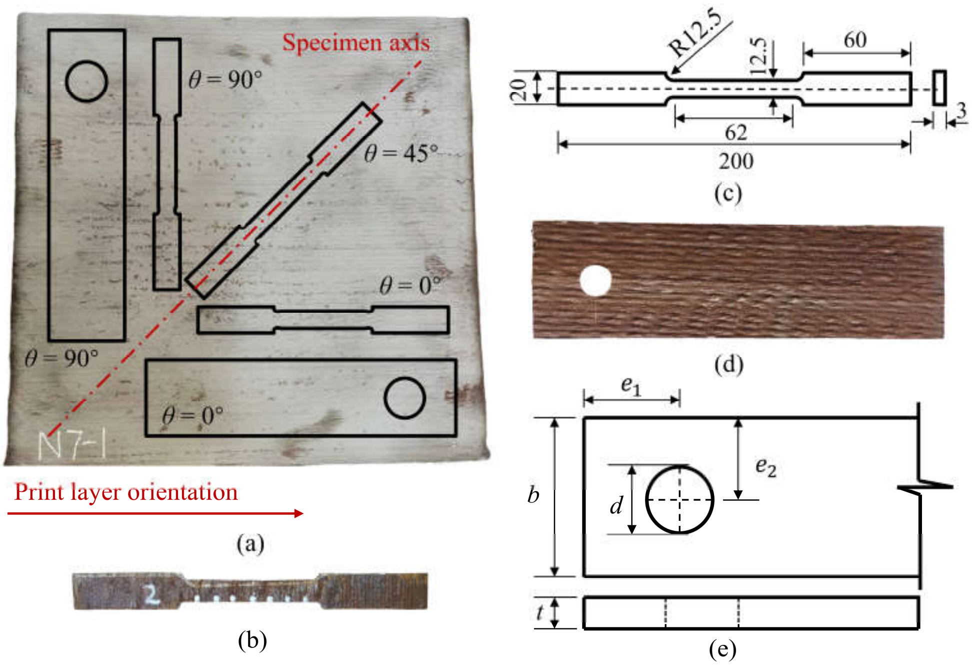

Figure 2. (a) Specimens extraction diagram from oval tubes with flat sides; (b) coupon with a θ of 90°; (c) dimensions of the coupon; (d) bolted connection specimen with a θ of 0°; and (e) dimensions of the bolted connection specimen.

Table 1. Chemical compositions (% by weight) of ER50-6 low carbon steel feedstock.

Chemical compositions	C	Mn	Si	P	S	Cr	Ni	Cu	Mo	V
ER50-6	0.074	1.47	0.85	0.015	0.01	0.023	0.009	0.1	0.004	0.002

Table 2. Mechanical properties of ER50-6 low carbon steel feedstock.

	Tensile Strength (MPa)	Yield Strength (MPa)	Elongation Rate (%)	Charpy V Impact Test Value at 40℃ (J)

ER50-6	554	445	26	96

Table 3. Printing and environmental parameters of specimens with a nominal thickness of 3 mm.

Travel speed (m/min)	Wire feed rate (m/min)	Wire diameter (mm)	Welding voltage (V)	Layer thickness (mm)	Bead width (mm)	Temperature (°C)	Humidity (%RH)	Shielding gas
0.65-0.7	4.0	1.2	19.5	1.8	5	12-21	35-55	97%Ar+ 3%CO_2

To investigate the effects of print layer orientations, tensile coupons were extracted from flat plates with three relative angles θ between the specimen axes and the print layer orientations of 0°, 45°, and 90°, as shown in Figure 2(a). In total, 24 tensile coupons (Figure 2(b)) with a nominal thickness of 3 mm were designed with the dimensions shown in Figure 2(c), including 6 coupons with θ being 0°, 6 coupons with θ being 45°, and 12 coupons with θ being 90°.

The masses and volumes of the WAAM tensile coupons were obtained using an electronic scale and Archimedes' principle respectively. An average density value of 7692 kg/m^3 was measured using masses dividing matched volumes. The obtained density was lower than 7850 kg/m^3 of conventional low-carbon steel, which was in consistence with the experimental work conducted at Imperial College London [10]. The lower density could be attributed to the pores generated during the WAAM production process [49, 50].

Meanwhile, 36 WAAM steel bolted connection specimens of a nominal thickness of 3 mm were extracted from the oval tubes with two θ values (0° and 90°), as shown in Figure 2(a). Each specimen plate (Figure 2(d)) was named in the form of HS-d-b-e_1 or VS-d-b-e_1 with nominal dimensions, such as HS-18-30-27. The letter 'H' or 'V' means that the plate was extracted horizontally or vertically to the print layer orientation, with θ being 0° or 90°, respectively. The letter 'S' means the single-shear connection type. As shown in Figure 2(e), the nominal diameter of the bolt hole and the nominal width of the bolted connection plate are represented by d and b, respectively. The letter e_1 is the minimum distance from the centre of the bolt hole to the end of the bolted connection plate.

High-strength Q690 steel plates with a nominal thickness of 4 mm were used to replace parts of WAAM steel plates in the bolted connections, to simplify the experimental variables and to ensure the failure occurring on the WAAM plates. Grade 12.9 high strength bolts and nuts were selected to prevent bolts from failing before the steel plates failed. The material properties of the high-strength Q690 steel plates were tested under the test setup shown in Figure 3(a) and the measured constitutive relationships are shown in Figure 3(b) and Table 4.

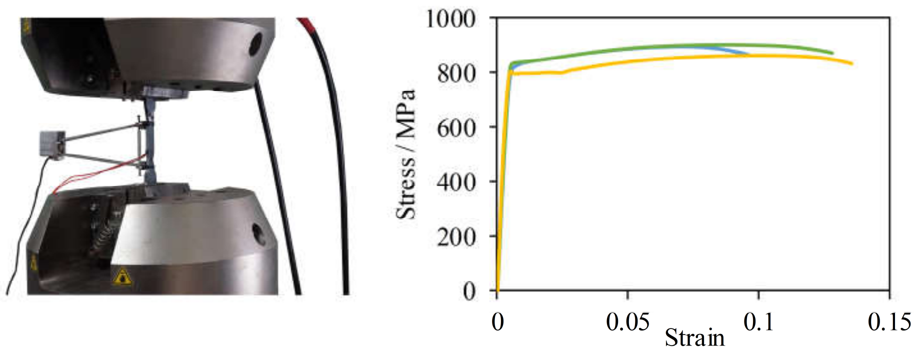

(a) (b)

Figure 3. (a) Test setup, and (b) measured stress-strain curves for Q690 steel plates.

Table 4. Material properties of Q690 steel plates.

Specimens	Nominal thickness (mm)	Actual thickness (mm)	E (GPa)	f_y (MPa)	f_u (MPa)	ε_u	ε_f
1		4.3	237	819	896	0.07	0.10
2	4	4.2	217	835	901	0.09	0.13
3		4.2	199	803	862	0.10	0.16
Average	4	4.2	218	819	886	0.09	0.12

Note: E: Young's modulus; f_y: yield stress; f_u: ultimate tensile stress; ε_u: ultimate tensile strain, and ε_f: fracture strain.

2.2 Geometric measurements

All the WAAM steel specimens had undulating surfaces, as shown in Figures 2(b) and (d). Therefore, it is almost impossible to measure the dimensions using traditional tools such as the vernier calliper or micrometre calliper. To measure the geometric information of the specimens in detail, a SIMSCAN 3D laser scanner was employed. The scanner can reach the maximum scanning rate of 2020000 measurements per second, with an accuracy of 0.02 mm and a maximum resolution of 0.025 mm. As shown in Figure 4, the selected laser scanner can sufficiently capture the main geometric characteristics with the maximum resolution of 0.025 mm.

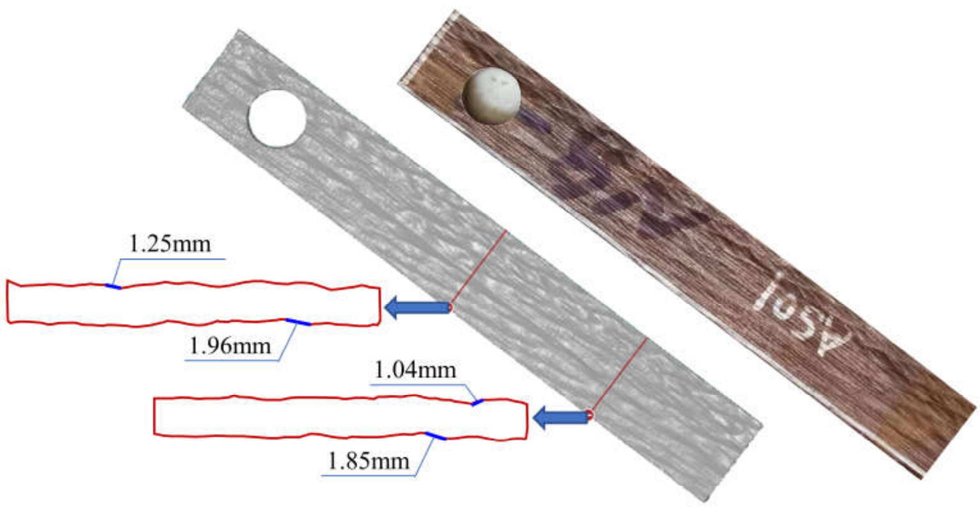

Figure 4. Surface undulation of the WAAM steel plates.

Figure 5 shows the whole scanning and measuring process. The test specimens were set up on a flat table with calibration markers. The scan data was recorded in the form of point clouds and imported into GOM Inspect for subsequent model post-processing such as eliminating grid errors and repairing imperfections in the digital model. The volumes of the specimens can therefore be measured via the digital models.

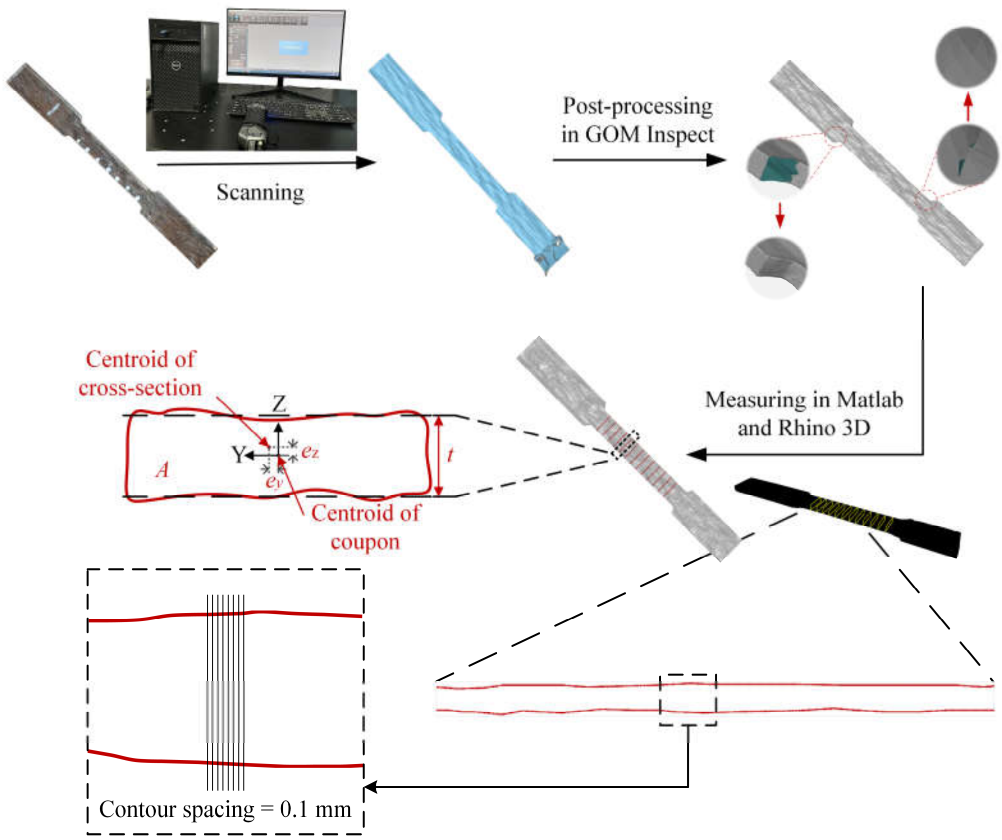

Figure 5. Scanning and measurement process of the WAAM plates.

To verify the accuracy of the scanner, the mass of each specimen was also recorded and its corresponding actual volume was calculated using the measured density value of 7692 kg/m^3. The differences between the scanned volumes and measured volumes via the mass/density were consistently within 2%, which verified the accuracy of the digital models.

Further geometric measurements were conducted based on a Matlab program [10] corresponding with Rhino 3D, which was developed by Imperial College London to calculate the geometric properties of the WAAM steel specimens with inherent surface undulations. The digital model without mesh errors and holes was first reoriented. The overall centroid of the specimens coincided with the origin of the global coordinate system, with the plane of the specimen paralleling to the XY plane, and the longitudinal axis of the specimens paralleling to the X-axis. After the alignment operation, several closed polygons representing the rectangular cross-sections were obtained by intersecting the specimen with planes in the same spacings perpendicular to the X-axis.

A sensitivity study on the contour spacing was conducted, to accurately reflect the geometric properties of the coupons while ensuring computational efficiency. Nine coupons were selected for the sensitivity analysis (three for each print layer orientation), and the contour spacings were set thinner than the typical WAAM bead widths [51] as 0.05 mm, 0.1 mm, 0.5 mm, 1 mm, and 2 mm.

The geometric properties calculated in various contour spacings were normalized according to the results obtained with dx = 0.05 mm. Figure 6 shows the results of the sensitivity analysis with various spacings, indicating that the average geometric properties (A, t, and e_z) were more sensitive to the contour spaces than the extreme geometric properties (A_{min}, t_{min}, and $e_{z,max}$). It can be found that the geometric properties with a spacing of 0.1 mm were similar to that of 0.05 mm. Hence, dx = 0.1 mm was taken as the contour spacing value due to higher computational efficiency.

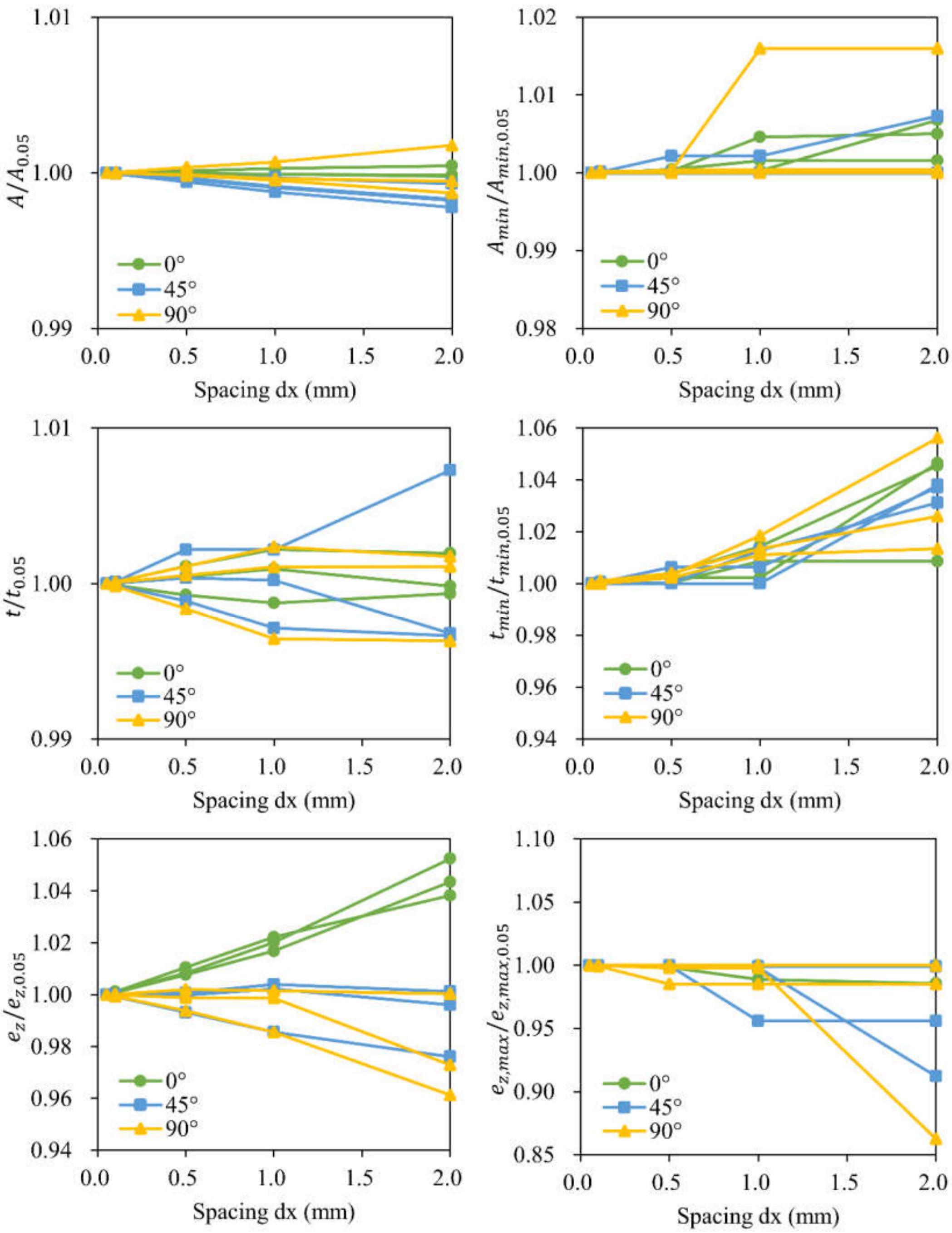

Figure 6. Results of sensitivity study on different spacings.

For each coupon test specimen, the cross-section profiles were extracted from the parallel segments of the specimens which were obtained from the process described above. Based on the geometric measurement approach shown in Figure 5, the geometric results of the coupon test specimens are shown in Table 5. The A_{std} and t_{std} values of the coupons with a θ of 0° were the minimum among three print layer orientation coupons, indicating the least variation in cross-sectional area and thickness along the X-axis. This is because all cross-sections perpendicular to the direction of the deposition paths are similar. In contrast, the dimensions of coupons with θ of 45° and 90° varied more in cross-sections. The average and maximum centroid eccentricities normalised by the corresponding average coupon thickness t, as well as their corresponding normalised standard deviations, increased with θ. Moreover, the eccentricities measured on the Y-axis were generally slightly higher than those on the Z-axis.

Table 5. Geometric properties of the WAAM coupons obtained from the analysis.

t_{nom} (mm)	θ (°)	A (mm^2)	A_{min} (mm^2)	A_{std} (mm^2)	t (mm)	t_{std} (mm)	$\frac{\lvert e_y \rvert}{t}$	$\frac{\lvert e_{y,max} \rvert}{t}$	$\frac{\lvert e_{y,std} \rvert}{t}$	$\frac{\lvert e_z \rvert}{t}$	$\frac{\lvert e_{z,max} \rvert}{t}$	$\frac{\lvert e_{z,std} \rvert}{t}$
3	0	42.3	40.8	0.80	3.4	0.25	0.03	0.07	0.02	0.01	0.04	0.01
	45	44.3	39.7	3.09	3.6	0.42	0.05	0.15	0.04	0.04	0.12	0.03
	90	41.1	36.7	2.38	3.3	0.29	0.05	0.16	0.04	0.05	0.14	0.04

Note: t_{nom} represents the nominal thickness of the coupons; A, A_{min}, and A_{std} represent the average, minimum, and standard deviation values of the cross-sectional area along the X-axis; t and t_{std} represent the average and standard deviation values of thickness; e_y, $e_{y,max}$, and $e_{y,std}$ represent the average, maximum, and standard deviation values of the eccentricity between the centroid of coupon and cross-section along the Y-axis; e_z, $e_{z,max}$, and $e_{z,std}$ represent the average, maximum, and standard deviation values of the eccentricity along the Z-axis.

Meanwhile, for each bolted connection specimen, cross-section profiles were extracted from full-length specimens to represent its final measurement results. The obtained average measurements of the WAAM steel bolted connection specimens and high-strength Q690 steel bolted connection specimens are shown in Table 6 and Table 7, respectively. The high-strength Q690 steel bolted connection specimens were named following the same form of WAAM steel bolted connection specimens. "HSS" means high-strength steel. The Q690 HSS plates with numbers “1” and “2” in Table 7 correspond to the WAAM steel plates with 0° and 90° print layer orientations, respectively. The minimum distance from the centre of a bolt hole to the edge of a bolted connection specimen was denoted as e_2. The thickness t varied from 2.9 mm to 3.5 mm, the width b varied from 30.2 mm to 69.8 mm, and the ratio of e_1 to e_2 varied from 0.5 to 1.8. The diameter of the bolt hole was d while the nominal bolt diameter was denoted as d_f.

Table 6. Geometric measurement results of WAAM steel plates.

Specimens	t (mm)	d_f (mm)	d (mm)	b (mm)	e_1 (mm)	e_1/e_2
HS-18-30-27	3.1	16.0	17.8	30.3	26.6	1.8
HS-18-40-27	3.4	16.0	18.2	39.6	27.8	1.4
HS-18-60-20	3.0	16.0	18.0	60.4	21.8	0.7
HS-18-70-22	3.3	16.0	17.6	69.5	20.8	0.6
HS-18-60-18	3.4	16.0	17.8	60.3	15.4	0.5
HS-18-60-22	3.3	16.0	17.8	60.4	21.6	0.7
HS-18-60-32	3.1	16.0	18.0	59.9	30.2	1.0
HS-18-60-36	3.0	16.0	17.8	60.3	35.0	1.2
HS-18-70-36	3.4	16.0	18.0	69.6	37.2	1.1
HS-22-40-33	3.3	20.0	21.6	39.6	32.4	1.6
HS-22-50-33	3.5	20.0	21.6	50.8	31.0	1.2
HS-22-50-36	3.0	20.0	21.6	50.8	35.2	1.4
HS-22-60-26	3.1	20.0	21.6	60.3	27.4	0.9
HS-22-60-40	3.1	20.0	21.8	60.3	37.6	1.2
HS-26-50-39	3.4	24.0	26.2	50.9	39.4	1.5
HS-26-70-47	3.1	24.0	26.0	69.4	46.8	1.3
HS-26-60-29	2.9	24.0	26.2	60.6	27.8	0.9
HS-26-70-45	3.1	24.0	26.4	69.2	44.3	1.3
VS-18-30-27	3.3	16.0	18.0	30.2	26.4	1.7
VS-18-40-27	3.4	16.0	17.8	39.7	26.1	1.3
VS-18-50-20	3.1	16.0	17.6	50.7	19.8	0.8
VS-18-70-22	3.2	16.0	17.6	69.5	22.2	0.6
VS-18-60-18	3.2	16.0	18.0	60.2	17.8	0.6
VS-18-60-22	3.1	16.0	18.0	60.4	21.2	0.7
VS-18-60-32	3.5	16.0	17.8	60.2	30.7	1.0
VS-18-60-36	3.1	16.0	17.8	60.4	35.5	1.2
VS-18-70-36	3.3	16.0	18.0	69.9	35.2	1.0
VS-22-40-33	3.3	20.0	21.0	39.6	32.5	1.6

VS-22-50-33	3.1	20.0	21.6	49.8	32.2	1.3
VS-22-50-36	3.1	20.0	21.6	51.0	35.0	1.4
VS-22-60-26	3.2	20.0	21.6	60.3	24.6	0.8
VS-22-60-40	3.2	20.0	21.6	60.2	38.4	1.3
VS-26-50-39	3.1	24.0	21.6	49.7	38.6	1.6
VS-26-70-47	3.1	24.0	26.2	69.6	45.9	1.3
VS-26-60-29	3.2	24.0	26.4	60.5	27.6	0.9
VS-26-70-45	3.1	24.0	26.0	69.8	44.6	1.3

Table 7. Geometric measurement results of High-strength Q690 steel plates.

Specimens		t (mm)	d_f (mm)	d (mm)	b (mm)	e_1 (mm)
HSS-18-30-27	1	4.0	16.0	18.0	31.2	26.1
	2	4.0	16.0	17.9	32.5	27.2
HSS-18-40-27	1	4.0	16.0	17.7	41.1	27.1
	2	4.0	16.0	17.5	41.4	24.7
HSS-18-60-20	1	4.0	16.0	17.5	61.4	19.3
	2	4.0	16.0	17.5	61.4	21.2
HSS-18-70-22	1	4.0	16.0	17.6	71.2	22.2
	2	4.0	16.0	17.7	71.6	22.3
HSS-18-60-18	1	4.0	16.0	17.5	60.7	17.8
	2	4.0	16.0	17.5	61.0	17.0
HSS-18-60-22	1	4.0	16.0	17.4	60.3	22.5
	2	4.0	16.0	17.4	61.5	22.4
HSS-18-60-32	1	4.0	16.0	18.1	61.3	33.0
	2	4.0	16.0	17.5	61.4	31.5
HSS-18-60-36	1	4.0	16.0	17.8	61.4	36.1
	2	4.0	16.0	17.3	60.9	35.3
HSS-18-70-36	1	4.0	16.0	17.9	71.4	35.8
	2	4.0	16.0	17.6	72.0	36.0
HSS-22-40-33	1	4.0	20.0	21.7	41.4	33.8
	2	4.0	20.0	21.9	40.9	33.3
HSS-22-50-33	1	4.0	20.0	22.1	51.3	32.9
	2	4.0	20.0	22.8	50.9	32.3
HSS-22-50-36	1	4.0	20.0	21.5	50.7	36.0
	2	4.0	20.0	21.9	51.7	36.5
HSS-22-60-26	1	4.0	20.0	22.6	61.3	26.8
	2	4.0	20.0	23.3	61.1	26.6
HSS-22-60-40	1	4.0	20.0	22.9	61.3	41.2
	2	4.0	20.0	23.4	61.5	40.4
HSS-26-50-39	1	4.0	24.0	25.9	51.0	38.5
	2	4.0	24.0	25.4	50.8	37.9

HSS-26-70-47	1	4.0	24.0	25.9	70.6	46.6
	2	4.0	24.0	25.3	70.7	46.6
HSS-26-60-29	1	4.0	24.0	26.3	60.7	28.8
	2	4.0	24.0	25.8	61.3	29.1
HSS-26-70-45	1	4.0	24.0	25.9	71.0	45.3
	2	4.0	24.0	25.9	71.0	45.3

Note: the measured geometric dimensions were obtained using Vernier calliper and micrometre calliper.

2.3 Test Arrangements

A total of 24 coupon tests and 36 bolted connection tests were conducted using a 250 kN Instron 8802 testing machine under displacement control mode until fracture. The tensile coupons were tested at a constant stroke rate of 0.8 mm/min while the bolted connection specimens were tested at a stroke rate of 1.0 mm/min at room temperatures (20–25 °C) referring to the test arrangements of other researchers [52-54]. The bolted connection tests were stopped after reaching the ultimate load [55]. The loading details could be referred to the test by Huang et al. [56].

The bolted connection specimen was composed of a WAAM steel plate and a matched high-strength steel plate, connected by a high-strength bolt. The bolted connection specimens were vertically clamped on the tensile machine, as shown in Figure 7(a). Auxiliary plates were added at the clamping end to load the bolted connection specimens under concentric load. The contact between the bolts and steel plates was at the threaded portion of the bolt shank. All bolt nuts were finger tightened.

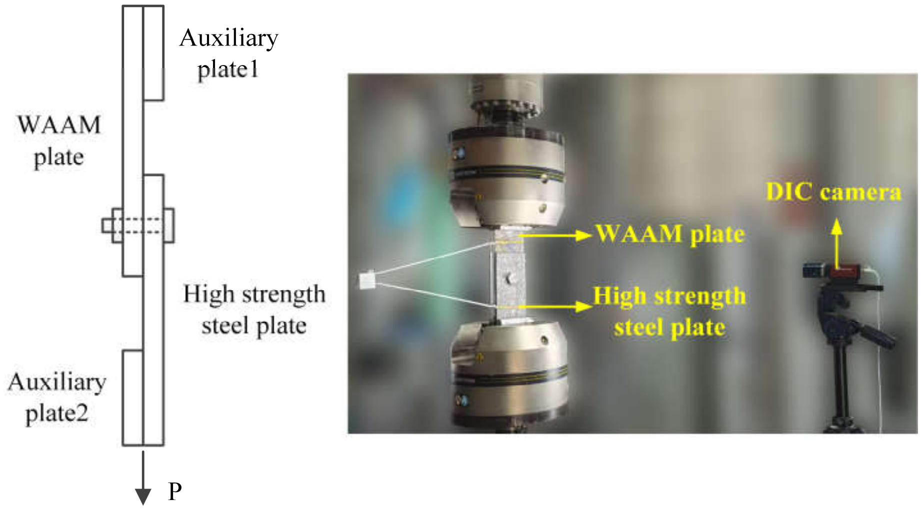

(a) (b)

Figure 7. Schematic diagram of the experimental setup: (a) bolted connection and (b) typical test arrangement for bolted connections.

Due to the difficulty of installing strain gauges on the undulating surfaces of the WAAM steel plates, a non-contact full-field measurement method based on the Digital Image Correlation (DIC) technique, was adopted to produce a more detailed response field compared with traditional measurement methods [57]. Figure 7(b) shows the typical bolted connection test arrangement in the Instron testing machine with a DIC-based device. The speckle pattern was generated by spraying the surface of specimens with white and black paints. Calibration markers were also attached to the surface of specimens for DIC calibration. To obtain accurate correlation analysis results, the specimens were installed in a straight and parallel direction to the camera sensor, and the camera was set vertically to the ground. The acquired images were recorded at a frequency of 5 Hz.

Both the conventional extensometer and DIC were set up to measure the displacement data, providing reliable verifications between each other. The conventional extensometer was fixed to the specimen and clamped with rubber bands. Specifically, the extensometer with a gauge length of 50 mm was utilized for the coupons. For the bolted connection tests, a larger extensometer with a gauge length of 150 mm was employed to measure the displacement between the two connection lap plates.

3. Test Results

3.1 Observations for tensile coupon tests

The material properties of the coupons were calculated based on the average cross-sectional area (Table 5), with a subscript of "effective" added to the symbols, such as E_{eff}. The average and the stress-strain curves of all WAAM tensile coupons with θ of 0°, 45°, and 90° are shown in Figure 8. The average effective material properties, Young's modulus E_{eff}, yield stress $f_{y,eff}$, ultimate tensile stress $f_{u,eff}$, ultimate tensile strain $\varepsilon_{u,eff}$, and fracture strain $\varepsilon_{f,eff}$, derived from stress-strain curves are shown in Table 8.

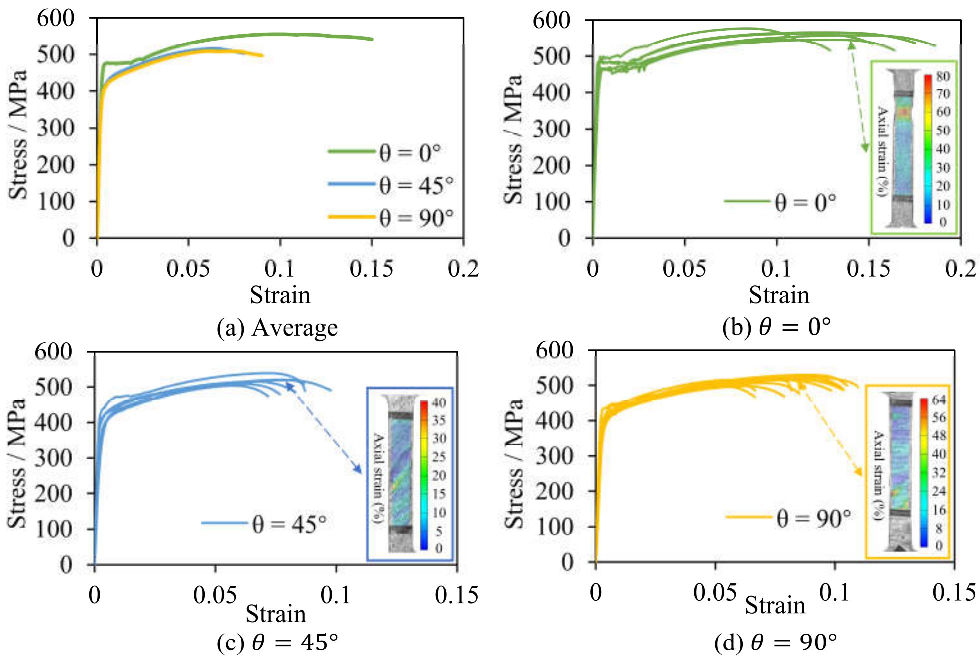

Figure 8. (a) Average stress-strain curves, and all stress-strain curves of WAAM tensile coupons with a

θ of (b) 0°, (c) 45°, and (d) 90°.

Table 8. Average material properties for WAAM tensile coupons.

t_{nom} (mm)	t (mm)	θ (°)	E_{eff} (GPa)	$\frac{E_{eff}}{E_{eff,0°}}$	$f_{y,eff}$ (MPa)	$\frac{f_{y,eff}}{f_{y,eff,0°}}$	$f_{u,eff}$ (MPa)	$\frac{f_{u,eff}}{f_{u,eff,0°}}$	$\varepsilon_{u,eff}$	$\frac{\varepsilon_{u,eff}}{\varepsilon_{u,eff,0°}}$	$\varepsilon_{f,eff}$	$\frac{\varepsilon_{f,eff}}{\varepsilon_{f,eff,0°}}$
	3.4	0	189	1.00	476	1.00	559	1.00	0.11	1.00	0.15	1.00
3	3.6	45	214	1.13	412	0.87	518	0.93	0.07	0.64	0.08	0.53
	3.3	90	198	1.05	408	0.86	515	0.92	0.07	0.64	0.09	0.60

Note: $E_{eff,0°}$, $f_{y,eff,0°}$, $f_{u,eff,0°}$, $\varepsilon_{u,eff,0°}$, and $\varepsilon_{f,eff,0°}$ is the average effective Young's modulus, yield stress, ultimate tensile stress, ultimate tensile strain, and fracture strain of WAAM tensile coupons with a θ of 0°.

Figures 8(b), (c), and (d) show the typical fractured coupons with different print layer orientations, along with the axial strain distributions visualised by the DIC system at the point of fracture. It was observed that the strain fields clearly reflected the starting point of the fractures and the print layer orientation of the coupons. Due to the undulating shapes, the coupons exhibited non-uniform strain fields with significant numerical fluctuations, but their average strains were consistent with the strains reflected by the extensometer within the gauge length.

From the stress-strain curves in Figure 8, it is shown that coupons with a θ of 0° had a clear yielding point. However, the other coupons did not have an explicit yielding phase. As a result, the yield stress was taken as the 0.2% proof stress. Figure 8 and Table 8 show that Young's modulus fluctuated at around 200 GPa. The average Young's modulus of the three groups of specimens with θ of 0°, 45°, and 90° were 189, 214, and 198 GPa, respectively, which could be influenced by the print layer orientations. Except for Young’s modulus, the other material properties of specimens with a θ of 45° and 90° were consistently lower than those of specimens with a θ of 0°, with differences of up to 13% and 14% for the yield stresses, 7% and 8% for the ultimate stresses, 36% and 36% for the ultimate tensile strain, and 47% and 40% for the fracture strain respectively, which showed anisotropic material properties of the WAAM steel plates. Very limited difference in the material properties of specimens with θ of 45° and 90° was found and it was the reason for the print layer orientations selected for the bolted connection tests with WAAM steel plates.

3.2 Observations from bolted connection tests

Four different failure modes, including net section, shear-out, end-splitting, and tilt-bearing failure, were observed from the tests, as presented in Figure 9.

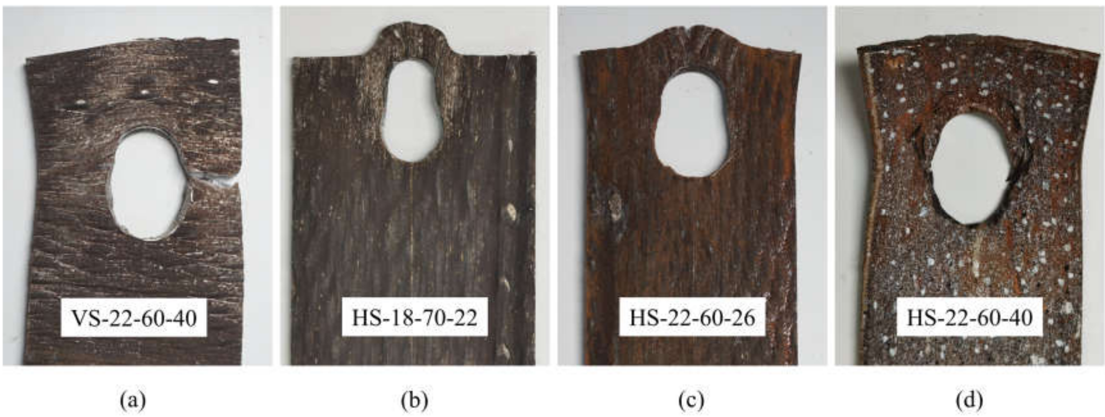

Figure 9. Examples of failure modes: (a) net section, (b) shear-out, (c) end-splitting, and (d) tilt-bearing.

Net section failure developed in 12 bolted connection specimens with a small width (or net width), considering that a small net section couldn't resist a large tensile action. It was observed that an initial crack developed at the centre of the bolt hole, and a necking run across the net section of the bolted connection plates, as shown in Figure 9(a). Figures 10(a) and (b) show the load-displacement curves of specimens with net section failure for the bolted connections extracted from different print layer orientations. The load-displacement curves usually had one ultimate point, and the load declined after reaching the ultimate capacity.

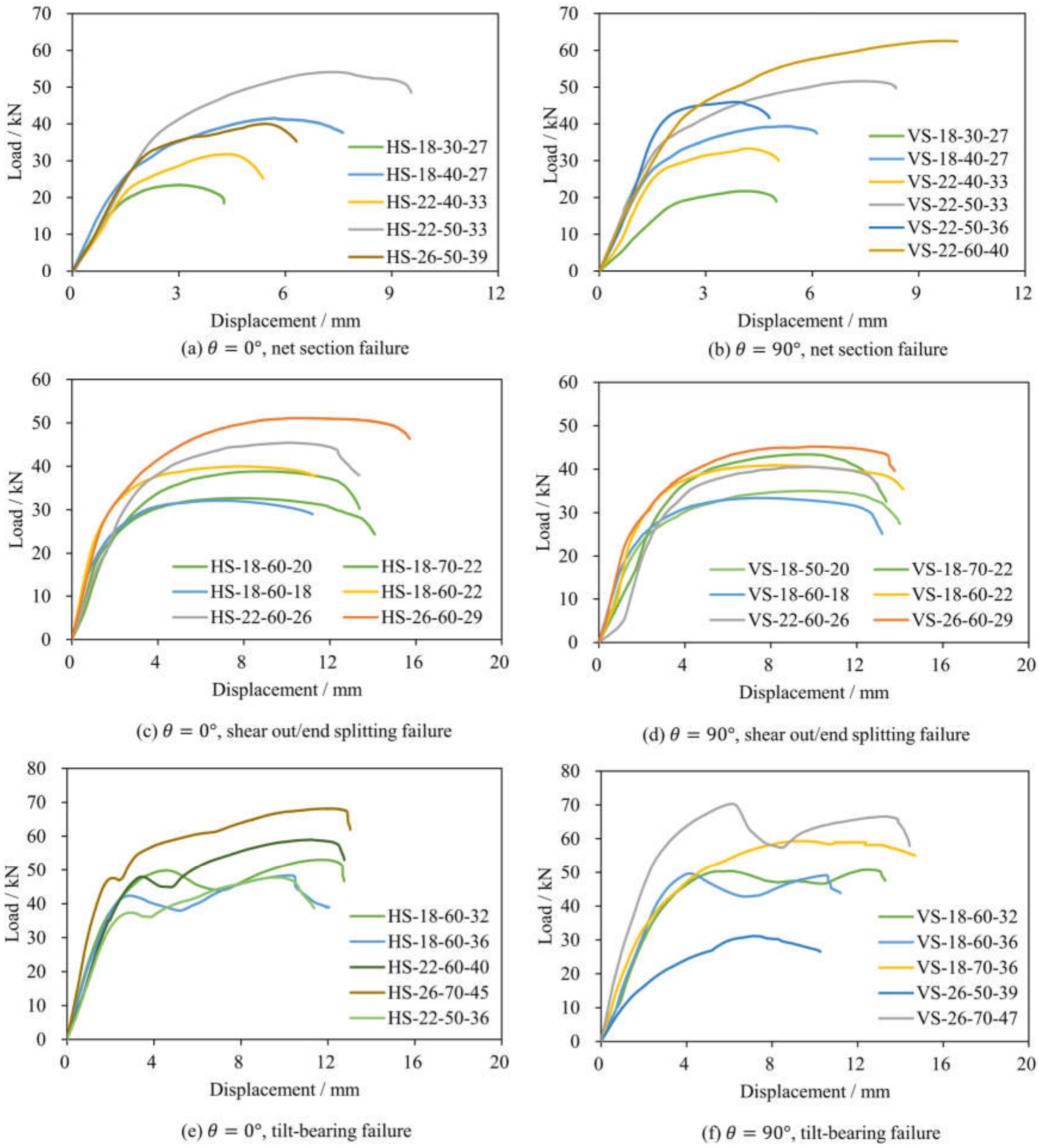

(a) $\theta = 0°$, net section failure

(b) $\theta = 90°$, net section failure

(c) $\theta = 0°$, shear out/end splitting failure

(d) $\theta = 90°$, shear out/end splitting failure

(e) $\theta = 0°$, tilt-bearing failure

(f) $\theta = 90°$, tilt-bearing failure

Figure 10. Load-displacement curve of WAAM steel bolted connection specimens failed at different failure modes.

The bolted connection plates with small end distances e_1 cannot provide sufficient shear resistance with the limited shear planes, resulting in the shear-out failure for 10 bolted connection specimens, as shown in Figure 9(b). It was also observed from Figures 10(c) and (d) that every curve had an obvious platform. In the test process, it was observed that the materials piled up in the front of the bolts until progressive fracture occurred and the materials were pushed out.

Only 3 specimens showed end-splitting failure in the tests, including HS-18-60-20, HS-22-60-26, and VS-26-60-29. As shown in Figure 9(c), end-splitting failure is characterised by rotation of net cross-section and transverse tensile fracture originating from the plate end. The axial strain ε_{yy} fields and transverse strain ε_{xx} fields visualised by the DIC system for specimen HS-22-60-26 are displayed in Figure 11. The colours of stress distributions were adjusted to make it more convenient to compare the strains in two directions. It was observed that the high transverse strain ε_{xx} was the controlling factor for end-splitting failure. The load-displacement curves of specimens with end-splitting failure were incorporated into the shear-out failure curves due to their similar failure behaviours, as shown in Figures 10(c) and (d).

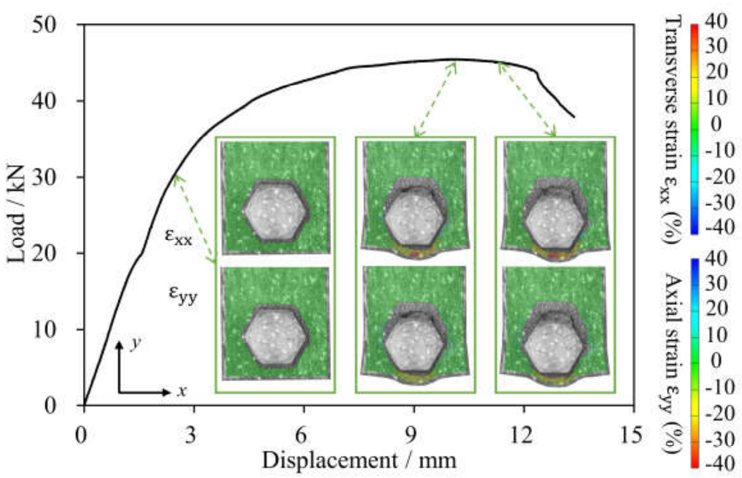

Figure 11. Strain fields at different displacements for specimen HS-22-60-26.

Different from specimen VS-22-60-26, which failed by pure shear-out, specimen HS-22-60-26 exhibited a combination of shear-out and end-splitting failure. A similar failure mode was also observed in the tests by Jiang et al. [58]. It presented both a tensile fracture at the tip of the specimen and a shear fracture along the elongation area, as shown in Figure 12, which could be attributed to high transverse strain ε_{xx} and axial strain ε_{yy} distributed in the specimen, simultaneously.

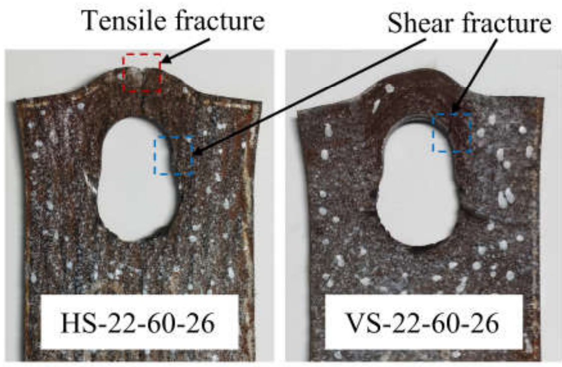

Figure 12. Comparison between specimens HS-22-60-26 and VS-22-60-26.

Tilt-bearing failure mode was observed in 12 specimens with the bolt head punching through the upstream side of the bolt hole, bolt tilting, and plate curling, as shown in Figure 9(d). Figure 10(e) and (f) show the typical load-displacement curves of the bolted connections corresponding to tilt-bearing failure mode. The curves usually had two peaks, and the first peak was related to the curl of the plate. The axial strain ε_{yy} fields at different displacements obtained by the DIC system for specimen HS-22-60-40 are displayed in Figure 13. The plate began to curl after the first peak, and the axial tensile strain ε_{yy} in the downstream of the bolt hole gradually increased as the stress was increased. Due to the presence of a bolt head, the strain and fracture in the upstream of bolt hole cannot be clearly observed. Individual curves had only one peak, even though the specimens still curled. Pure bearing failure was not discovered due to the eccentricity of the applied load in the single shear connections.

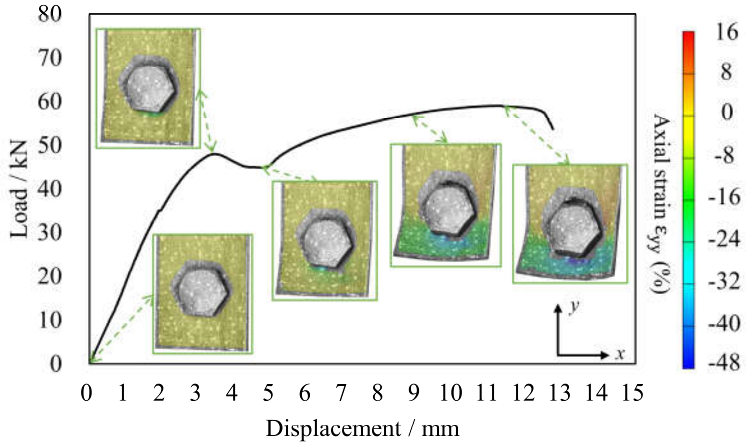

Figure 13. Strain fields at different displacements for specimen HS-22-60-40.

The print layer orientation had impacts on the responses of the bolted connection specimens, including failure modes and ultimate capacities. Among all pairs of specimens with similar dimensions but different print layer orientations, 29% of the pairs of specimens encountered different failure modes. As shown in Figure 14, the 5 pairs of specimens showed different failure modes in a total of 17 pairs of specimens, mainly including 4 pairs of different failures of net section failure and tilt-bearing failure, and one pair of different failures of shear-out failure and end-splitting failure. The VS specimens tended to present net section failure instead of tilt-bearing failure, except for VS-26-50-39. However, they all followed the trend that the specimens with net section failure had higher ultimate capacities and larger deformation than those of specimens with tilting-bearing failure. HS-26-60-29 and VS-26-60-29 showed shear-out failure and end-splitting failure respectively, and the former had a higher ultimate capacity and larger deformation.

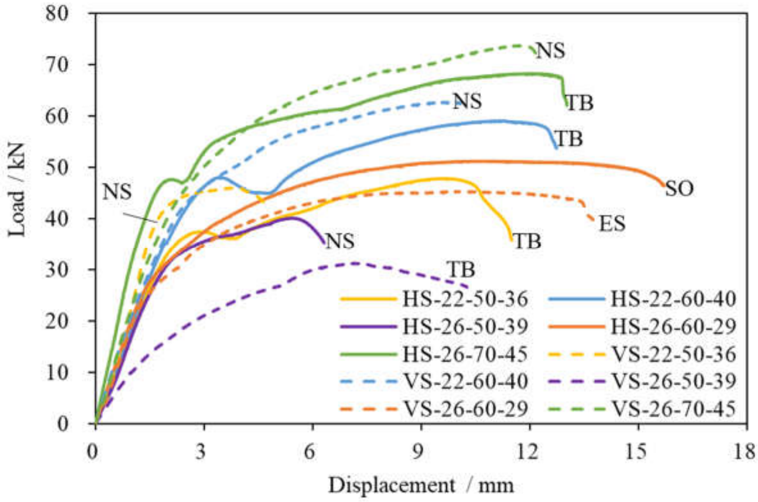

Figure 14. Load-displacement curves of the specimens with similar dimensions in different print layer orientations resulting in different failure modes.

The normalised ultimate capacities $P_{u,0°}/tf_{u,eff,0°}$ and $P_{u,90°}/tf_{u,eff,90°}$ of the HS and VS WAAM steel bolted connection specimens are compared in Figure 15. The ratios of $P_{u,90°}/tf_{u,eff,90°}$ and $P_{u,0°}/tf_{u,eff,0°}$ were within the range from 0.8 to 1.2, indicating that the differences in the ultimate capacity of the HS and VS specimens of the bolted connection tests were within 20%. This showed that the ultimate capacities in the bolted connection tests were sensitive to the print layer orientations. The red triangles in Figure 15 represent the five pairs of specimens with different failure modes mentioned in the previous section. The triangles were distributed differently without special rules, which could be attributed to the limited specimens being tested and further experimental investigations are required in the future.

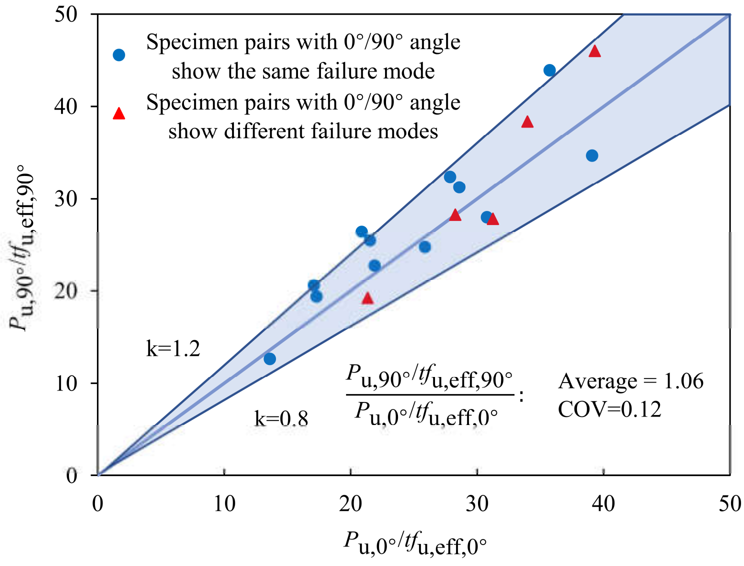

Figure 15. Comparison of different print layer orientations on ultimate capacities of bolted connection tests.

4. Design codes

The development of accurate and reliable design stipulations is important for the wider application of WAAM structures in the construction industry. In this section, the ultimate capacities of the tested specimens were evaluated against the predictions provided by the design rules stipulated in available design standards, namely AS/NZS 4600 [27], AS 4100 [28], AISI S100 [29], AISC 360 [30], EN 1993-1-1 [31], EN 1993-1-3 [32], and EN 1993-1-8 [33]. The proposed design rules from the recent literature were also evaluated with the test results to assess their suitability for the WAAM steel bolted connection design.

4.1 AS/NZS 4600 & AS 4100

4.1.1 AS/NZS 4600:2018 [27]

The ultimate capacities corresponding to different failure modes of a single bolt connection in the cold-formed sheet are specified in AS/NZS 4600:2018 [27]. When bearing capacities are calculated without considering bolt hole deformation, the nominal tensile capacity $P_{ns,NZS}$ of the net section of the connection plate is:

$$P_{\mathrm{ns,NZS}} = [0.9 + (\frac{0.1d_{\mathrm{f}}}{b})]A_{\mathrm{n}}f_{\mathrm{u}} \tag{1}$$

where, d_f is the nominal bolt diameter; b is the width of the plate in the bolted connection; A_n is net sectional area of the connection plate; and f_u denotes the tensile strength of the connection plate.

The nominal shear-out capacity $P_{so,NZS}$ of the connection plate is:

$$P_{\mathrm{so,NZS}} = e_1 t f_{\mathrm{u}} \tag{2}$$

where, t is the thickness of the connection plates; and e_1 is the distance between the centre of a standard bolt hole to the end of the connection plate.

The nominal bearing capacity $P_{b,NZS}$ of the connection plate is:

$$P_{\mathrm{b,NZS}} = \alpha C d_{\mathrm{f}} t f_{\mathrm{u}} \tag{3}$$

where, α = a modification factor, α is set as 0.75 for the single shear bolted connection without washers; C = bearing factor, when d_f/t < 10, C = 3.0; when 10 < d_f/t < 22, C = 4 – 0.1(d_f/t); and when d_f/t > 22, C = 1.8.

4.1.2 AS 4100:2020 [28]

The ultimate capacities of cold-formed steel bolted connections corresponding to various failure modes are specified in AS 4100:2020 [28]. When bearing capacities are calculated without considering bolt hole deformation, the nominal tensile capacity $P_{ns,AS}$ of the net section of the connection plate is:

$$P_{\mathrm{ns,AS}} = 0.85A_{\mathrm{n}}f_{\mathrm{u}} \tag{4}$$

The nominal shear-out capacity $P_{\mathrm{so,NZS}}$ of the connection plate is:

$$P_{\mathrm{so,AS}} = (e_1 - \frac{d}{2})tf_{\mathrm{u}} \tag{5}$$

where, d is the nominal bolt hole diameter.

The nominal bearing capacity $P_{\mathrm{b,NZS}}$ of a bolted connection is:

$$P_{\mathrm{b,AS}} = 3.2d_{\mathrm{f}}tf_{\mathrm{u}} \tag{6}$$

4.2 AISI S100& AISC 360

4.2.1 AISI S100:2016 [29]

The ultimate capacities of a bolted connection in the cold-formed sheet are specified in AISI S100:2016 [29]. When the bearing capacities are calculated without considering bolt hole deformation, the nominal tensile capacity $P_{\mathrm{ns,AISI}}$ of the net section and the nominal bearing capacity $P_{\mathrm{b,AISI}}$ of the connection plate is the same as AS/NZS 4600:2018 [27], following Equation (1) and (3). The nominal shear-out capacity $P_{\mathrm{so,AISI}}$ of the connection plate is:

$$P_{\mathrm{so,AISI}} = 1.2(e_1 - \frac{d}{2})tf_{\mathrm{u}} \tag{7}$$

4.2.2 AISC 360:2022 [30]

The load-carrying capacities of a single bolt connection corresponding to various failure modes in cold-formed sheets are also specified in AISC 360:2020 [30]. The nominal tensile capacity $P_{\mathrm{ns,AISC}}$ of the net section of a connection plate is:

$$P_{\mathrm{ns,AISC}} = A_{\mathrm{n}} f_{\mathrm{u}} \tag{8}$$

The nominal shear-out capacity $P_{\mathrm{so,AISC}}$ of the connection plate is:

$$P_{\mathrm{so,AISC}} = 1.5(e_1 - \frac{d}{2}) t f_{\mathrm{u}} \tag{9}$$

The nominal bearing capacity $P_{\mathrm{b,AISC}}$ of the connection plate is:

$$P_{\mathrm{b,AISC}} = 3 d_{\mathrm{f}} t f_{\mathrm{u}} \tag{10}$$

4.3 Eurocode

4.3.1 EN 1993-1-1:2020 [31]

The nominal tensile capacity $P_{\mathrm{ns,EN1}}$ of the net section of a connection plate determined by EN 1993-1-1:2020 [31], is shown in Equation (11), which is also incorporated into EN 1993-1-8:2021 [33] for connection design.

$$P_{\mathrm{ns,EN1}} = k A_{\mathrm{n}} f_{\mathrm{u}} \tag{11}$$

where, $k = 1$, for plates with smooth holes fabricated by drilling or water jet cutting, or $k = 0.9$, for plates with rough holes fabricated by punching or flame cutting.

4.3.2 EN 1993-1-3:2022 [32]

According to EN 1993-1-3:2022 [32], the nominal tensile capacity $P_{\mathrm{ns,EN3}}$ of the net section of the connection plate is:

$$P_{\mathrm{ns,EN3}} = (1 + 3(\frac{d}{b} - 0.3)) A_{\mathrm{n}} f_{\mathrm{u}} \tag{12}$$

where, $(1+3(d/b-0.3)) \leqslant 1$.

The nominal tensile capacity P_{EN3} of the shear out and bearing of the connection plate is

$$P_{\mathrm{EN3}} = 2.5\alpha_{\mathrm{b}} k_{\mathrm{t}} d_{\mathrm{f}} t f_{\mathrm{u}} \tag{13}$$

where, α_b is the minimum value of 1 and $e_1/3d_f$; when 0.75 mm< t <1.25 mm, k_t = (0.8t+1.5)/2.5, and when t > 1.25 mm, k_t = 1.

4.3.3 EN 1993-1-8:2021 [33]

According to EN 1993-1-8:2021 [33], the nominal tensile capacity P_{EN8} of the shear out and bearing of the connection plate is:

$$P_{\mathrm{EN8}} = \alpha_{\mathrm{b}} k_{\mathrm{m}} d_{\mathrm{f}} t f_{\mathrm{u}} \tag{14}$$

where, α_b is the minimum of e_1/d, $3f_{ub}/f_u$, and 3; for steel grades equal to or higher than S460, k_m = 0.9; otherwise k_m = 1.

4.4 Design equations proposed in the literature

Teh and Uz [37] modified Eq. (7) by proposing an active shear length, L_{av}, instead of a net shear length, where $L_{av} = e_1 - d/4$.

$$P_{\mathrm{so}} = 1.2(e_1 - \frac{d}{4}) t f_{\mathrm{u}} \tag{15}$$

A modification of Eq. (16) had been proposed by Xing et al. [35] considering the catenary action which has a significant effect on the shear out capacity.

$$P_{\mathrm{so}} = 1.2(\frac{3d_{\mathrm{f}}}{e_1})^p (e_1 - \frac{d}{4}) t f_{\mathrm{u}} \tag{16}$$

where, p = the influence degree of catenary action, taken as 1/10 herein for the single-shear single-bolt connections.

Lyu et al. [45] proposed a new Eq. (17) for the prediction of ultimate bearing capacity taking into account splitting failure. The reduction factor φ varies in the value of e_1/d, but their relationship shows a complicated feature. The reduction factor was recommended as φ = 0.9 [45].

$$P_{\mathrm{so}} = \begin{cases} 1.04\dfrac{e_1}{d} d_{\mathrm{f}} t f_{\mathrm{u}}, e_1/e_2 \leq 0.5 \\ \varphi P_{\mathrm{so}}, e_1/e_2 > 0.5 \end{cases} \tag{17}$$

Equation (18) was also proposed for determining the ultimate tilt-bearing capacity [46], which is distinguished from the conventional bearing failure.

$$P_{\mathrm{tb}} = 2.65(b - d) d_{\mathrm{f}}^{\frac{1}{2}} t^{\frac{4}{3}} f_{\mathrm{u}} \tag{18}$$

5. Comparisons between test results and various design equations

5.1 Failure mode comparison results

The standards were used to calculate the ultimate capacities related to different failure modes including net section, shear-out, and bearing failures, according to the size information of the specimens. The failure mode corresponding to the lowest ultimate capacity was considered as the failure mode predicted by the standards. The experimental results of the failure mode were compared with the predictions following the design approaches, as shown in Appendix A.

The overall prediction accuracies of the six standards for failure modes were not very satisfying. The highest accuracy rate was acquired by AISC 360 [30] and AS/NZS 4600 [27], reaching 0.61, as shown in Figure 16. Part of the reason is that tilt-bearing and end-splitting failure are not involved in the standards, which led to the wrong judgment of failure modes when the experimental failure modes were tilt-bearing and end-splitting failure. It is suggested that the future design codes or guidelines specialised for 3D printed steel structures should involve the two failure modes that have not been specified in current design provisions.

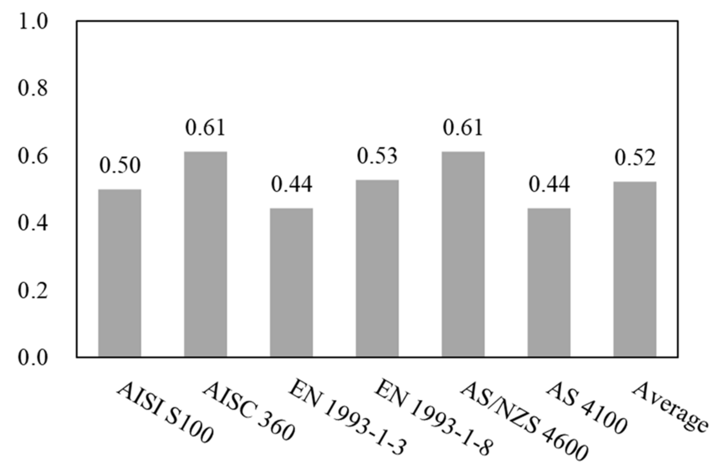

Figure 16. Prediction accuracies of failure modes in six standards.

5.2 Ultimate capacities comparing with various design methods

The experimental results of ultimate tensile capacities were compared with the predictions following the design approaches reviewed in Appendix A. In general, the design standards presented showed different degrees of underestimation with the mean of test-to-predicted capacity ratio $P_{\mathrm{exp}}/P_{\mathrm{pre}}$ varying from 1.03 to 1.48.

AS/NZS 4600 [27] performed the best in the six standards with both the lowest average test-to-predicted capacity ratio of 1.03 and a coefficient of variation (COV) of 0.11. The underestimation of the ultimate capacity of the connections was only 3%. Whilst, AS 4100 [28] was the least accurate and stable with the highest underestimation of the ultimate load-carrying capacity by 32% with a COV of 0.27.

To evaluate the applicability of the existing design approaches on WAAM steel bolted connections, further analysis will be conducted in the following sections corresponding to different failure modes. The prediction accuracy of the design approaches proposed in the current literature for a particular failure mode will be discussed in Sections 5.3-5.6.

5.3 Net section failure

Figure 17 presents the test-to-predicted capacity ratio and the coefficient of variation for various design codes of practice. When the failure mode of the WAAM steel plate was net section failure, the test-to-predicted capacity ratio predicted by each specification fluctuated between 1.01 and 1.27, and the COV lay between 0.07 and 0.11. The average predicted ultimate capacity of net section failure in AISC 360 [30] was the most accurate, reaching an average ratio of 1.00, with a COV of less than 0.07. The predictions of ultimate capacities for specimens with net section failure were generally accurate and stable, except for AS 4100 [28].

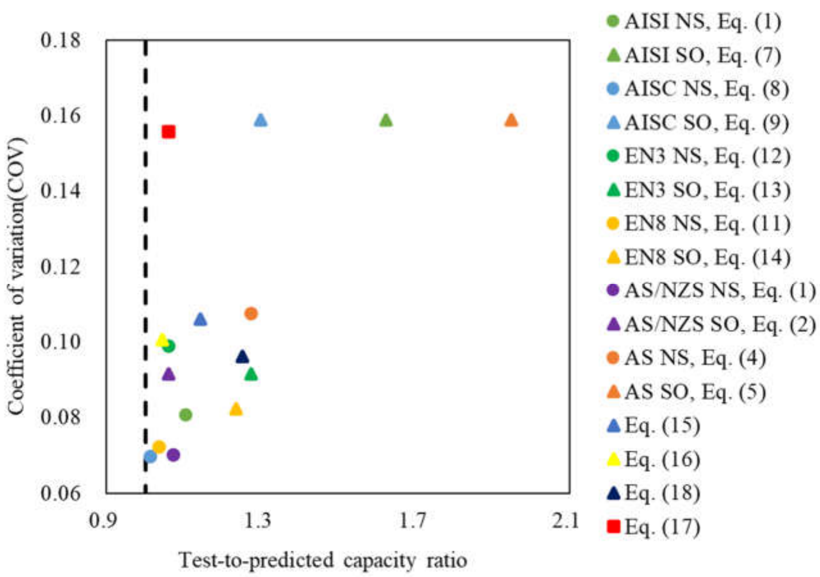

Figure 17. Evaluation of different codes towards different failure modes.

5.4 Shear-out failure

When the failure mode of the WAAM steel plate was a shear-out failure, the average test-to-predicted capacity ratio and COV changed significantly for various design standards. This was due to the different shear planes and shear coefficients used in the equations for shear-out failure. Among all the design standards, AS/NZS 4600 [27] and Equation (16) performed the best with an underestimation of 6% and 4%, with a COV of 0.09 and 0.10, respectively. The test-to-predicted capacity ratios of AISC 360 [30], AISI S100 [29], and AS 4100 [28] were larger than 1.30 and the test-to-predicted ratios were scattered, but their COVs were in good consistency. This is because all these equations use e_1-$d/2$ as the edge length of the shear plane, differing only in terms of shear coefficient. All equations caused underestimations ranging from 4% to 49%, which were much worse than the prediction of the specimens with net section failures.

5.5 End-splitting failure

The ultimate load-carrying capacity of end-splitting failure is usually lower than that of shear failure, which is important for 3D printed steel connections [45]. However, it is not stipulated in many design standards, which is often judged to be a shear-out failure, as shown in Appendix A.

In Equation (17), $e_1/e_2 = 0.5$ was used as the boundary of shear-out and end-splitting failure. When $e_1/e_2 > 0.5$, it was considered that end-splitting failure would occur, and a simple uniform reduction factor of 0.9 could be used based on the formula for shear-out failure [45]. It is worth noting that the dimensions of all specimens met the condition of $e_1/e_2 > 0.5$, but only three specimens presented end-splitting failure mode. This slightly affected the accuracy of Equation (17), resulting in an underestimation of 20% and a COV of 0.10. However, when the reduction factor was used for the three specimens, it resulted in the test-to-predicted ratio of 1.06, 1.09, and 1.19 respectively, which needs further research to improve it.

5.6 Tilt-bearing failure

The tilt-bearing failure has not been incorporated into the current design standards. Appendix A shows that different design standards calculated specimens with tilt-bearing failures as net section tension or shear-out failures, resulting in underestimation or overestimation of the tilt-bearing capacities.

Equation (18) was proposed to predict the capacities of the specimens failing in tilt-bearing. It related the bearing capacity of tilt-bearing failure to plate dimensions, such as net length b-d, bolt diameter d_f, and plate thickness t, which was consistent with the damage mechanism. It showed satisfactory with an underestimation of 6% and a COV of 0.16.

6. Conclusions

In this paper, a total number of 24 coupon specimens with 3 different print layer orientations and 36 single-shear connection specimens with 2 different print layer orientations and varying dimensions were tested. The geometric properties of WAAM steel specimens were calculated using a 3D laser scanner and a Matlab program. The measured material properties, geometries, load-deformation characteristics, and failure modes were reported and analysed. The test ultimate capacities were compared against the predictions of 6 available design standards and other design approaches proposed in recent literature. According to the observation of the experimental phenomenon and the analysis of the result data, the following conclusions can be drawn:

1) In the WAAM coupon tests, except for Young's modulus, most of the other material properties of specimens with a θ of 45° and 90° were consistently lower than those of specimens with θ of 0°, with differences of up to 10%, which showed anisotropic material properties of the WAAM steel plates. And the difference among the material properties of specimens with θ of 45° and 90° was limited.

2) Four different failure modes, including net section, shear-out, end-splitting, and tilt-bearing failure, were observed from the bolted connection tests. The print layer orientations (θ = 0° and 90°) influenced the failure modes and load-carrying capacities of the WAAM connections. Different failure modes were observed from 29% of the specimens with similar dimensions but different print layer orientations. The difference in the ultimate capacity of bolted connection specimens with θ of 0° and 90° reached up to 20%.

3) Current steel design standards cannot accurately predict the failure modes of WAAM steel bolted connection specimens with the accuracy rates varying from 44% to 61%. This could be attributed to the influence of anisotropic material properties of the WAAM steel plates and the failure modes of tilt-bearing and the end-splitting not being considered in current design provisions. The accurate predictions of the ultimate capacities of most design

approaches were obtained by a compromise of the incorrect failure modes of WAAM steel bolted connection specimens.

4) The ultimate load-bearing capacities of WAAM steel bolted connection specimens could be accurately predicted by the existing design standards, where AS/NZS 4600 [27] performed the best with a test-to-predicted capacity ratio of 1.03 and a COV of 0.11. In terms of different specific failure modes, the ultimate capacities of net section and shear-out failure were precisely predicted by AISC 360 [30] and AS/NZS 4600 [27].

5) The equations proposed in recent literature for shear-out and tilt-bearing failure could well predict the ultimate capacities with an underestimation of 4% and 6%, respectively. The equation for end-splitting failure was not suitable for WAAM steel bolted connection specimens. It is suggested that WAAM design methods for end-splitting failure should be further researched in the future.

Acknowledgement

The authors would like to thank the financial supports from the National Natural Science Foundation of China (NSFC) (Grant Number: 52208215), the Natural Science Foundation of Zhejiang Province (Grant Number: LQ22E080008) and the Centre for Balance Architecture of Zhejiang University. The author would also like to thank the code for WAAM geometry analysis provided by the Steel Structures Group of Imperial College London. The help for the tests from the technician Mr Xiaohua Ji from the Structures Lab is also appreciated.

Appendix

Appendix A. Summary of experimental results and comparisons with design codes.

Specimen	Test		AISI S100 (Eqs.1,3,7)		AISC 360 (Eqs.8-10)		EN 1993-1-3 (Eqs.12,13)		EN 1993-1-8 (Eqs.11,14)		AS/NZS 4600 (Eqs.1-3)		AS4100 (Eqs.4-6)		Eq.15	Eq.16	Eq.17	Eq.18
	FM	P_u (kN)	FM	$\frac{P_u}{P_{AISI}}$	FM	$\frac{P_u}{P_{AISC}}$	FM	$\frac{P_u}{P_{EN3}}$	FM	$\frac{P_u}{P_{EN8}}$	FM	$\frac{P_u}{P_{AS/NZS}}$	FM	$\frac{P_u}{P_{AS}}$	$\frac{P_u}{P_{TEH}}$	$\frac{P_u}{P_{XING}}$	$\frac{P_u}{P_{LYU}}$	$\frac{P_u}{P_{TEH}}$
HS-18-30-27	NS	23.44	NS	1.14	NS	1.09	NS	1.09	NS	1.09	NS	1.14	NS	1.28				
HS-18-40-27	NS	41.55	NS	1.09	NS	1.02	NS	1.02	NS	1.02	NS	1.09	NS	1.20				
HS-18-60-20	ES	32.70	SO	1.25	SO	1.00	SO	1.06	SO	1.10	SO	0.88	SO	1.50	0.93	0.86	1.06	
HS-18-70-22	SO	38.82	SO	1.45	SO	1.16	SO	1.20	SO	1.23	SO	1.00	SO	1.74	1.06	0.98	1.18	
HS-18-60-18	SO	32.10	SO	2.19	SO	1.75	SO	1.33	SO	1.37	SO	1.11	SO	2.63	1.30	1.16	1.32	
HS-18-60-22	SO	39.94	SO	1.41	SO	1.13	SO	1.20	SO	1.23	SO	1.00	SO	1.69	1.05	0.97	1.18	
HS-18-60-32	TB	52.99	SO	1.21	SO	0.97	SO	1.22	SO	1.27	SO	1.02	SO	1.45				1.07
HS-18-60-36	TB	48.36	SO	0.91	SO	0.73	SO	0.98	SO	1.01	SO	0.82	SO	1.10				1.00
HS-18-70-36	TB	74.97	SO	1.15	SO	0.92	SO	1.26	SO	1.31	SO	1.09	SO	1.39				1.27
HS-22-40-33	NS	31.75	NS	1.01	NS	0.96	NS	0.96	NS	0.96	NS	1.01	NS	1.13				
HS-22-50-33	NS	54.07	SO	1.15	NS	0.95	SO	1.08	SO	1.08	NS	1.01	SO	1.38				
HS-22-50-36	TB	47.68	NS	1.03	NS	0.97	NS	0.97	NS	0.97	NS	1.03	SO	1.16				0.94
HS-22-60-26	SO/ES	45.49	SO	1.30	SO	1.04	SO	1.13	SO	1.13	SO	0.94	SO	1.56	0.98	0.91	1.09	
HS-22-60-40	TB	58.96	SO	1.06	NS	0.88	SO	1.08	SO	1.09	NS	0.95	SO	1.27				1.07
HS-26-50-39	NS	40.08	NS	0.91	NS	0.86	NS	0.86	NS	0.86	NS	0.91	NS	1.02				
HS-26-70-47	TB	60.96	SO	0.88	NS	0.82	SO	0.92	SO	0.92	NS	0.88	SO	1.06				1.01

HS-26-60-29	SO	51.05	SO	1.77	SO	1.42	SO	1.35	SO	1.36	SO	1.12	SO	2.13	1.23	1.11	1.31	
HS-26-70-45	TB	68.19	SO	1.05	NS	0.92	SO	1.06	SO	1.08	NS	0.98	SO	1.26				1.11
VS-18-30-27	NS	21.81	NS	1.09	NS	1.04	NS	1.04	NS	1.04	NS	1.09	NS	1.23				
VS-18-40-27	NS	39.41	NS	1.11	NS	1.04	SO	1.05	NS	1.04	NS	1.11	SO	1.32				
VS-18-50-20	SO	34.98	SO	1.66	SO	1.33	SO	1.33	SO	1.22	SO	1.11	SO	2.00	1.19	1.09	1.30	
VS-18-70-22	SO	43.40	SO	1.64	SO	1.32	SO	1.43	SO	1.31	SO	1.19	SO	1.97	1.24	1.15	1.40	
VS-18-60-18	SO	33.40	SO	1.95	SO	1.56	SO	1.39	SO	1.30	SO	1.16	SO	2.34	1.29	1.17	1.39	
VS-18-60-22	SO	40.93	SO	1.74	SO	1.39	SO	1.44	SO	1.35	SO	1.20	SO	2.09	1.27	1.17	1.45	
VS-18-60-32	TB	50.80	SO	1.07	SO	0.86	SO	1.10	SO	1.02	SO	0.91	SO	1.29				0.93
VS-18-60-36	TB	49.64	SO	0.98	SO	0.78	SO	1.06	SO	0.98	SO	0.88	SO	1.18				1.08
VS-18-70-36	TB	59.37	SO	1.10	SO	0.88	SO	1.18	SO	1.11	SO	0.99	SO	1.32				1.13
VS-22-40-33	NS	33.31	NS	1.10	NS	1.04	NS	1.04	NS	1.04	NS	1.10	NS	1.23				
VS-22-50-33	NS	51.66	SO	1.26	NS	1.15	SO	1.21	NS	1.15	NS	1.22	SO	1.51				
VS-22-50-36	NS	45.76	NS	1.03	NS	0.96	SO	0.97	NS	0.96	NS	1.03	SO	1.17				
VS-22-60-26	SO	40.54	SO	1.50	SO	1.20	SO	1.21	SO	1.09	SO	1.01	SO	1.80	1.08	0.98	1.16	
VS-22-60-40	NS	62.59	SO	1.16	NS	0.99	SO	1.20	SO	1.08	NS	1.07	SO	1.39				
VS-26-50-39	TB	31.15	NS	0.73	NS	0.68	NS	0.68	NS	0.68	NS	0.73	NS	0.81				0.64
VS-26-70-47	TB	70.34	SO	1.12	NS	1.01	SO	1.15	SO	1.05	NS	1.08	SO	1.34				1.24
VS-26-60-29	ES	45.23	SO	1.61	SO	1.29	SO	1.21	SO	1.11	SO	1.01	SO	1.93	1.11	1.00	1.19	
VS-26-70-45	NS	73.61	SO	1.21	NS	1.05	SO	1.24	SO	1.12	NS	1.13	SO	1.46				1.29
FMPA			0.50		0.61		0.44		0.53		0.61		0.44					
Mean				1.25		1.06		1.13		1.10		1.03		1.48	1.14	1.04	1.25	1.06
COV				0.25		0.21		0.14		0.13		0.11		0.27	0.11	0.10	0.10	0.16

Note: FM = failure mode; NS: net section tension; SO: shear-out; ES: end-splitting; TB: tilt-bearing failure; FMPA: failure mode prediction accuracy and COV: coefficient of variation.

Reference

[1] Buchanan C, Gardner L. Metal 3D printing in construction: a review of methods, research, applications, opportunities and challenges. Engineering Structures. 2019;180:332-48.

[2] Duda T, Raghavan LV. 3D metal printing technology: the need to re-invent design practice. Ai & Society. 2018;33:241-52.

[3] Ding D, Pan Z, Cuiuri D, Li H. Wire-feed additive manufacturing of metal components: technologies, developments and future interests. The International Journal of Advanced Manufacturing Technology. 2015;81:465-81.

[4] Wu B, Pan Z, Ding D, Cuiuri D, Li H, Xu J et al. A review of the wire arc additive manufacturing of metals: properties, defects and quality improvement. Journal of Manufacturing Processes. 2018;35:127-39.

[5] Gardner L, Kyvelou P, Herbert G, Buchanan C. Testing and initial verification of the world's first metal 3D printed bridge. Journal of Constructional Steel Research. 2020;172:106233.

[6] Feucht T, Waldschmitt B, Lange J, Erven M. Additive manufacturing of a bridge in situ. Steel Construction. 2022;15:100-10.

[7] Zuo W, Chen M, Chen Y, Zhao O, Cheng B, Zhao J. Additive manufacturing oriented parametric topology optimization design and numerical analysis of steel joints in gridshell structures. Thin-Walled Structures. 2023;188:110817.

[8] Ye J, Kyvelou P, Gilardi F, Lu H, Gilbert M, Gardner L. An end-to-end framework for the additive manufacture of optimized tubular structures. IEEE Access. 2021;9:165476-89.

[9] Ermakova A, Mehmanparast A, Ganguly S, Razavi N, Berto F. Investigation of mechanical and fracture properties of wire and arc additively manufactured low carbon steel components. Theoretical and Applied Fracture Mechanics. 2020;109:102685.

[10] Huang C, Kyvelou P, Zhang R, Ben Britton T, Gardner L. Mechanical testing and microstructural analysis of wire arc additively manufactured steels. Materials & Design. 2022;216:110544.

[11] Kyvelou P, Slack H, Buchanan C, Wadee MA, Gardner L. Material testing and analysis of WAAM stainless steel. 2021;4:1702-9.

[12] Kyvelou P, Slack H, Daskalaki Mountanou D, Wadee MA, Britton TB, Buchanan C et al. Mechanical and microstructural testing of wire and arc additively manufactured sheet material. Materials & Design. 2020;192:108675.

[13] Lin Z, Goulas C, Ya W, Hermans MJM. Microstructure and mechanical properties of medium carbon steel deposits obtained via wire and arc additive manufacturing using metal-cored wire. Metals. 2019;9:673.

[14] Sun L, Jiang F, Huang R, Yuan D, Guo C, Wang J. Anisotropic mechanical properties and deformation behavior of low-carbon high-strength steel component fabricated by wire and arc additive manufacturing. Materials Science and Engineering: A. 2020;787:139514.

[15] Guo C, Liu M, Hu R, Yang T, Wei B, Chen F et al. High-strength wire + arc additive manufactured steel. International Journal of Materials Research. 2020;111:325-31.

[16] Hadjipantelis N, Weber B, Buchanan C, Gardner L. Description of anisotropic material response of wire and arc additively manufactured thin-walled stainless steel elements. Thin-Walled Structures. 2022;171:108634.

[17] Buchanan C, Real E, Gardner L. Testing, simulation and design of cold-formed stainless steel CHS columns. Thin-Walled Structures. 2018;130:297-312.

[18] Laghi V, Palermo M, Gasparini G, Girelli VA, Trombetti T. Experimental results for structural design of wire-and-arc additive manufactured stainless steel members. Journal of Constructional Steel Research. 2020;167:105858.

[19] Kyvelou P, Huang C, Gardner L, Buchanan C. Structural testing and design of wire arc additively manufactured square hollow sections. Journal of Structural Engineering. 2021;147:04021218.

[20] Huang C, Meng X, Buchanan C, Gardner L. Flexural buckling of wire arc additively manufactured tubular columns. Journal of Structural Engineering. 2022;148:04022139.

[21] Huang C, Meng X, Gardner L. Cross-sectional behaviour of wire arc additively manufactured tubular beams. Engineering Structures. 2022;272:114922.

[22] Guo X, Kyvelou P, Ye J, Gardner L. Experimental investigation of wire arc additively manufactured steel T-stub connections. Journal of Constructional Steel Research. 2023;211:108106.

[23] Ye J, Quan G, Yun X, Guo X, Chen J. An improved and robust finite element model for simulation of thin-walled steel bolted connections. Engineering Structures. 2022;250:113368.

[24] Ye J, Quan G, Kyvelou P, Teh L, Gardner L. A practical numerical model for thin-walled steel connections and built-up members. Structures. 2022;38:753-64.

[25] Quan G, Ye J, Li W. Computational modelling of cold-formed steel lap joints with screw fasteners. Structures. 2021;33:230-45.

[26] Winter G. Tests on bolted connections in light gage steel. Journal of the Structural Division. 1956;82:920-1.

[27] AS/NZS 4600. Cold-formed steel structures. Sydney: Australian/New Zealand Standard; 2018.

[28] AS 4100. Steel structures. Australia: Standards Association of Australia; 2020.

[29] AISI S100. North American specification for the design of cold-formed steel structural

members. Washington DC: American Iron and Steel Institue; 2016.

[30] AISC 360. Specification for structural steel buildings. Chicago: American Institute of Steel Construction; 2022.

[31] Eurocode 3: design of steel structures – part 1-1: general rules and rules for builidng. Brussels: European Committee for Standardisation; 2020.

[32] Eurocode 3 - design of steel structures - part 1-3: general rules - supplementary rules for cold-formed members and sheeting. Brussels: European Committee for Standardisation; 2022.

[33] Eurocode 3: design of steel structures – part 1-8: design of joints. Brussels: European Committee for Standardisation; 2021.

[34] Bhuiyan RA, Ahmed A, Teh LH. Ultimate bearing capacity of unconfined bolted connections in cold-formed steel members. Journal of Structural Engineering. 2021;147:04021048.

[35] Xing H, Teh LH, Jiang Z, Ahmed A. Shear-out capacity of bolted connections in cold-reduced steel sheets. Journal of Structural Engineering. 2020;146:04020018.

[36] Clements DDA, Teh LH. Active shear planes of bolted connections failing in block shear. Journal of Structural Engineering. 2013;139:320-7.

[37] Teh LH, Uz ME. Ultimate shear-out capacities of structural-steel bolted connections. Journal of Structural Engineering. 2015;141:04014152.

[38] Teh LH, Gilbert BP. Net section tension capacity of bolted connections in cold-reduced steel sheets. Journal of Structural Engineering. 2012;138:337-44.

[39] Salih EL, Gardner L, Nethercot DA. Numerical investigation of net section failure in stainless steel bolted connections. Journal of Constructional Steel Research. 2010;66:1455-66.

[40] Salih EL, Gardner L, Nethercot DA. Bearing failure in stainless steel bolted connections. Engineering Structures. 2011;33:549-62.

[41] Kim TS, Kuwamura H, Kim S, Lee Y, Cho T. Investigation on ultimate strength of thin-walled steel single shear bolted connections with two bolts using finite element analysis. Thin-Walled Structures. 2009;47:1191-202.

[42] Soo Kim T, Kuwamura H. Finite element modeling of bolted connections in thin-walled stainless steel plates under static shear. Thin-Walled Structures. 2007;45:407-21.

[43] Kim TS, Kuwamura H, Cho TJ. A parametric study on ultimate strength of single shear bolted connections with curling. Thin-Walled Structures. 2008;46:38-53.

[44] Wang YB, Lyu YF, Li GQ, Liew JYR. Behavior of single bolt bearing on high strength steel plate. Journal of Constructional Steel Research. 2017;137:19-30.

[45] Lyu YF, Wang YB, Li GQ, Jiang J. Numerical analysis on the ultimate bearing resistance

of single-bolt connection with high strength steels. Journal of Constructional Steel Research. 2019;153:118-29.

[46] Teh Lip H, Uz Mehmet E. Ultimate tilt-bearing capacity of bolted connections in cold-reduced steel sheets. Journal of Structural Engineering. 2017;143:04016206.

[47] Ding C, Torabian S, Schafer BW. Strength of bolted lap joints in steel sheets with small end distance. Journal of Structural Engineering. 2020;146:04020270.

[48] Guo X, Kyvelou P, Ye J, Teh LH, Gardner L. Experimental investigation of wire arc additively manufactured steel single-lap shear bolted connections. Thin-Walled Structures. 2022;181:110029.

[49] Tonelli L, Laghi V, Palermo M, Trombetti T, Ceschini L. AA5083 (Al–Mg) plates produced by wire-and-arc additive manufacturing: effect of specimen orientation on microstructure and tensile properties. Progress in Additive Manufacturing. 2021;6:479-94.

[50] Hu Q, Miao J, Wang X, Li C, Fang K. Microstructure and properties of ER50-6 steel fabricated by wire arc additive manufacturing. Scanning. 2021;2021:7846116.

[51] Ding DH, Pan ZX, Dominic C, Li HJ. Process planning strategy for wire and arc additive manufacturing. Robotic Welding, Intelligence and Automation. 2015:437-50.

[52] Chen M, Young B. Tensile tests of cold-formed stainless steel tubes. Journal of Structural Engineering. 2020;146:04020165.

[53] Chen M, Zhang T, Young B. Behavior of concrete-filled cold-formed steel built-up section stub columns. Thin-Walled Structures. 2023;187:110692.

[54] Chen M, Cai A, Pandey M, Shen C, Zhang Y, Hu L. Mechanical properties of high strength steels and weld metals at arctic low temperatures. Thin-Walled Structures. 2023;185:110543.

[55] Rogers CA, Hancock GJ. Failure modes of bolted-sheet-steel connections loaded in shear. Journal of Structural Engineering. 2000;126:288-96.

[56] Huang Y, Young B. The art of coupon tests. Journal of Constructional Steel Research. 2014;96:159-75.

[57] Pan B. Digital image correlation for surface deformation measurement: historical developments, recent advances and future goals. Measurement Science and Technology. 2018;29:082001.

[58] Jiang B, Yam MCH, Ke K, Lam ACC, Zhao Q. Block shear failure of S275 and S690 steel angles with single-line bolted connections. Journal of Constructional Steel Research. 2020;170:106068.